Wall-locking of kink modes in a line-tied screw pinch with a rotating wall

C. Paz-Soldan, M. I. Brookhart, C. C. Hegna, and C. B. Forest

Related Articles

Additional information on Phys. Plasmas

Wall-locking of kink modes in a line-tied screw pinch with a rotating wall[a)]

C. Paz-Soldan,[b)] M. I. Brookhart, C. C. Hegna, and C. B. Forest

Physics Department, University of Wisconsin-Madison, Madison, Wisconsin 53706, USA

The effect of rotating conducting walls on mode-locking is studied in a line-tied, linear screw pinch experiment and then compared to a torque balance model which has been extended to include differential wall rotation. Wall rotation is predicted to asymmetrically affect the mode-unlocking threshold, with fast rotation eliminating the locking bifurcation. Static error fields are observed to lock the resistive wall mode (RWM) variant of the current driven kink instability by modifying the electromagnetic torque. Using locked modes, the stabilizing effect of wall rotation on the RWM is experimentally demonstrated by illustrating a reduction of the RWM growth rate and an extension of the RWM-stable operation window. © *2012 American Institute of Physics.*
[http://dx.doi.org/10.1063/1.3694521]

I. INTRODUCTION

The resistive wall mode (RWM) is a performance-limiting magneto-hydrodynamic (MHD) instability[2] which is commonly excited when current in the reversed-field pinch[3] or pressure in the tokamak[4,5] exceed critical values.[6] The RWM grows when stabilizing eddy currents in a conducting wall Ohmically dissipate, allowing flux to penetrate on the time scale of the wall's resistive diffusion ($\tau_w \equiv \mu_0 \sigma_w r_w \delta_w$, where σ_w, r_w, and δ_w are the wall conductivity, radius, and thickness, respectively).

Plasma flow is also important to RWM stability,[7] as MHD modes entrained in a rapidly flowing plasma can rotate with frequency $\omega \gg \tau_w^{-1}$. These fast modes see the wall as ideal and cannot become RWMs. In toroidal configurations, RWMs in slowly rotating plasmas can also be stabilized by kinetic resonances with trapped particle populations.[8,9] Furthermore, small deviations from the design axisymmetric magnetic field (termed "error fields") can interact with the RWM, usually by applying an electromagnetic braking torque to the plasma.[10] In certain regimes, the RWM discontinuously transitions from a rotationally stabilized RWM to a stationary ($\omega \approx 0$) "locked" RWM followed by subsequent fast growth with $\gamma^{-1} \propto \tau_w$.[11] For this reason, experimental observations of RWM onset conditions are often convolutions of RWM stability criteria and mode-locking thresholds.[11] Theoretically, mode-locking has generally been treated as a competition between viscous and electromagnetic torques,[12–17] with the resulting equations resembling those of an induction motor.[18] Although mode-locking was historically studied in the context of tearing modes,[19] similar equations can be written for the RWM.[10] Theory also suggests[20–23] that a system of differentially rotating conducting walls can stabilize the RWM, as the RWM will always be rotating in the frame of one of the two walls. Stabilization by rotating walls is of interest due to its analogy to an infinite set of active coils[24] and the application

to future devices utilizing flowing liquid metals for cooling, tritium breeding, or the first wall.[25]

In this work, the effect of physically rotating walls on the RWM is tested experimentally and interpreted using a torque balance model that accounts for both field errors and wall rotation. Plasma rotation yields a kHz-scale rotating RWM which must be slowed or locked to observe the interaction of the instability with the rotating wall. Braking and locking are shown to be achieved with static $m = 0$ and $m = 1$ error fields, yielding the first observation of MHD mode-locking in a linear device. Here, m refers to the azimuthal mode number of the magnetic perturbation. These effects are interpreted with a commonly used torque balance model[12–14] which is adapted to this experiment. This model is further extended to treat differential wall rotation using the thin-wall, long-cylinder approximation. Wall rotation is found to Doppler shift the mode-locking threshold. However, a much larger effect is predicted for the mode-unlocking threshold, and asymmetry in wall rotation direction is also predicted. The extended model is then used to fit mode-locking observations in the presence of a rotating wall. Locked modes are shown to be successfully stabilized, with wall rotation found to reduce the RWM growth rate and saturated amplitude, and to extend the RWM-stable operation window. Initial RWM stabilization results are reported in Ref. 26, while in the present work, an extended explanation of the mode-locking observations is given in the context of a model torque balance expression.

Experiments are performed on the rotating wall machine,[1] a 1.2 m long by 16 cm diameter screw pinch (shown in Fig. 1), in which the RWM is robustly observed.[27] A uniform 500 G axial guide field (B_z) is applied by four external solenoids, and azimuthal field is provided by up to 7 kA of plasma current (I_p). Plasmas are generated by an array of 7 washer-stabilized hollow cathode plasma guns[28] which, when electrostatically biased with respect to an external anode, source both plasma and current. The bias on each gun is feedback controlled, allowing current profiles to be tailored in both space and time. The rotating wall itself is a precision-engineered 1 m long by 18 cm diameter stainless steel tube with a 1 mm interior copper
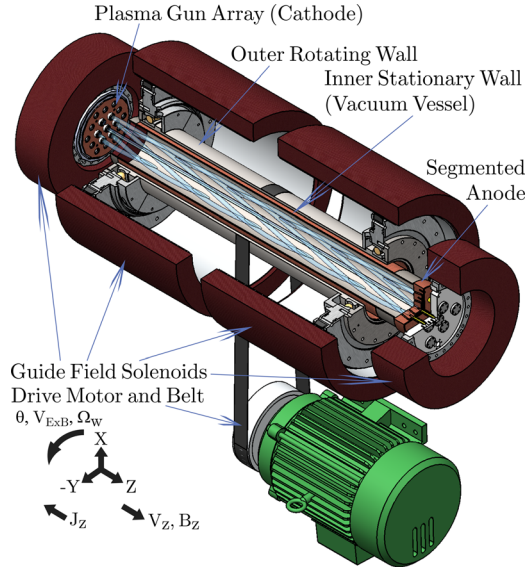

FIG. 1. The rotating wall machine[1] experimental geometry. Plasmas are illustrated as discrete flux-ropes, though measurements indicate that a fully merged axisymmetric profile is achieved by 1/3rd of the distance to the anode.

liner yielding $\tau_w = 7$ ms. The static wall (vacuum vessel) is also stainless steel with a 0.5 mm exterior copper liner yielding $\tau_w = 4$ ms. The relevant non-dimensional parameter describing rotation is the magnetic Reynolds number ($R_m \equiv \Omega_w \tau_w$, where Ω_w is the wall angular velocity) which sets the ratio of advection to diffusion of the magnetic field. Experiments here described are conducted up to $R_m = 5$, which corresponds to rotation at 260 km/h (6800 rpm). Unless otherwise noted, discharges presented throughout this paper contain 6.0 kA of I_p, with the central gun disengaged to generate a less peaked current profile. Langmuir probe measurements[29] indicate the plasma is dense ($n_e \approx 10^{20}$ m^{-3}) and uniformly cold ($T_e \approx$ 3–4 eV), with $n_e \propto I_p$, while T_e is insensitive to I_p. Measurements of MHD activity are made with a low-profile 8 axial by 10 azimuthal B_r edge flux-loop array located in between the static and rotating walls.

The structure of this paper is as follows: Sec. II derives and describes the torque balance equation used to model mode-locking in the experiment. Section III applies this model to describe experimental observations of mode-locking by $m = 0$ and $m = 1$ static error fields. Mode-locking in the presence of wall rotation is treated in Sec. IV, while Sec. V describes locked RWM stabilization by the rotating conducting wall. Discussion of results is presented in Sec. VI.

II. MODE-LOCKING MODEL AND FREE PARAMETERS

In order to model azimuthal RWM rotation in the experiment, total torques on a rigidly rotating plasma are calculated. Due to the high collisionality of the cold and dense plasma, the mode is taken to be fully entrained in the plasma flow such that the mode frequency ω is equal to the plasma rotation frequency ω. To simplify the analysis, the plasma is taken to be a rigid-rotor, such that everywhere the plasma rotates at a single frequency ω and $V_\theta = r\omega$. This approximation is equivalent to the large viscosity limit, as will be

discussed in Sec. VI. The total torques on the plasma can thus be evaluated,

$$
\hat{z} \cdot \int_{\mathcal{V}} \vec{r} \times \left[\rho \left(\frac{\partial \vec{V}}{\partial t} + \vec{V} \cdot \nabla \vec{V} \right) \right] d\mathcal{V}
$$
$$
= \hat{z} \cdot \int_{\mathcal{V}} \vec{r} \times \left[-\nabla p - \nabla \cdot \bar{\bar{\Pi}} + \nabla \cdot \bar{\bar{T}} \right] d\mathcal{V}, \qquad (1)
$$

where ρ is the density, p is the pressure, and $\bar{\bar{\Pi}}$ and $\bar{\bar{T}}$ are the viscous and Maxwell stress tensors, respectively. The integral is performed over a volume $\mathcal{V}$ enclosed by a cylindrical surface $\mathcal{S}$ of length L and radius r_a outside of the plasma but just inside the first wall. As $r_a/L \approx 10$, the large aspect ratio approximation allows the end-caps to be neglected due to their small contribution to $\mathcal{S}$. As $\mathcal{S}$ is outside the plasma, the pressure and viscous stress terms vanish. Using the rigid-rotor approximation, the advection term also vanishes. The inertial term is equal to $I_{zz}\dot{\omega}$, where I_{zz} is the moment of inertia of the rigidly rotating plasma and can be shown to be small relative to the remaining electromagnetic term. Using the divergence theorem and as the end caps are neglected in $\mathcal{S}$, the remaining term in Eq. (1) can be written as

$$
0 = r_a \int_{\mathcal{S}} \hat{\theta} \frac{1}{\mu_0} \left[\vec{B}\vec{B} - \frac{1}{2} B^2 \bar{\bar{I}} \right] d\mathcal{S}, \qquad (2)
$$

and as $\hat{\theta} \perp d\mathcal{S}$, the second term vanishes. The magnetic field is written as $\vec{B} = \vec{B}_0 + \vec{B}_{\text{ext}} + \tilde{B} \exp(-i\phi)$, where $\vec{B}_0$, $\vec{B}_{\text{ext}}$, $\tilde{B}$ are the equilibrium, error, and RWM field, respectively, and $\phi \equiv \int_0^t \omega(t')dt' + \phi_0$. $\vec{B}_0$ is taken to be axisymmetric ($m = 0$), while the $\vec{B}_{\text{ext}}$ and $\tilde{B}$ are non-axisymmetric ($m = 1$). Each magnetic field source produces a contribution to the torque balance relation, and these are calculated in Secs. II A–II C. Summing these contributions results in a torque balance of the form

$$
0 = \Gamma_{\text{res}} + \Gamma_{\text{ext}} + \Gamma_{EM} = A_{\text{res}}(\Omega_0 - \omega) + A_{\text{ext}} \sin(\phi)
$$
$$
- A_{EM} \frac{R_a R_b^2 \alpha^2 + 4(R_a + R_b(\alpha + 1))}{(4 + R_a R_b \alpha)^2 + 4(R_a + R_b)^2}, \qquad (3)
$$

where $\Gamma_{\text{res}}, \Gamma_{\text{ext}}$, and Γ_{EM} are the electromagnetic torques arising from the restoring torque to a "natural" frequency Ω_0, the mode-error field interactions, and the mode-wall interactions, respectively. Within $\Gamma_{EM}, R_a \equiv \omega\tau_a, R_b \equiv (\omega - \Omega_w)\tau_b, \alpha \equiv (r_a^2 - r_b^2)/r_b^2$, and τ_a, r_a, τ_b, r_b are the wall time and radius of the inner and outer wall, respectively, and Ω_w is the wall angular velocity. Γ_{ext} and Γ_{EM} can be measured using magnetic flux-loops,[30] leaving Ω_0 and A_{res} as the free parameters in the model. Equation (3) is quintic in ω and will be shown to be multi-valued, with rotating $\omega \approx \Omega_0$ and locked $\omega \approx 0$ solutions as well as bifurcations (mode-locking) between the two occurring at a critical ω_{lock} which can also be measured. The combined measurements of $\omega_{lock}, \Gamma_{EM}$, and Γ_{ext} are sufficient to uniquely determine both Ω_0 and A_{res}; thus, these parameters are not fit but rather calculated for a given discharge.

A. Derivation of two-wall electromagnetic torque

The electromagnetic torque from interactions of the RWM mode fields with the resistive wall is treated rigorously and can be directly measured experimentally.[30,31] The non-axisymmetric part of $\vec{B}$ in Eq. (2) will be considered and subsequently cycle-averaged. Cycle-averaging eliminates cross terms like $\vec{B}_{ext}\tilde{B}$, and these will be considered separately in Sec. II B. The integral to be evaluated is thus

$$\Gamma_{EM} = \frac{r_a^2 L}{\mu_0} \int_0^{2\pi} \langle \tilde{B}_\theta \tilde{B}_r \rangle d\theta, \tag{4}$$

where $\langle \cdots \rangle$ denotes a cycle-average. Note that integration in θ would drop terms that scale like $\vec{B}_0 \vec{B}_{ext}$ or $\vec{B}_0 \tilde{B}$. To compute Eq. (4), Laplace's equation in the long-cylinder approximation is solved, showing that the magnetic field in the vacuum region between the plasma and the wall must take the form

$$B_r(r,\theta) = \Re\left[(A_j - A_k r^{-2})e^{-i\theta}\right],$$
$$B_\theta(r,\theta) = \Re\left[(-i(A_j + A_k r^{-2}))e^{-i\theta}\right], \tag{5}$$

where A_j, A_k are complex coefficients. Computing Eq. (4) with this field structure yields

$$\Gamma_{EM} = \frac{r_a^2 \pi L}{\mu_0} \Im\left[\left(A_j - A_k r_a^{-2}\right)\left(A_j^* + A_k^* r_a^{-2}\right)\right]. \tag{6}$$

Note that there can be no torque unless there is both A_j and A_k, and that at least one of them is complex. The phase shift between B_r and B_θ at the wall must thus differ from $\pi/2$, which is accomplished by eddy currents induced in the wall when $\omega \neq 0$. Note that for this reason terms arising from non-axisymmetric static fields like $\vec{B}_{ext}\vec{B}_{ext}$ in Eq. (2) yield no net torque. To evaluate Eq. (6), the coefficients A_j, A_k must be determined from knowledge of the geometry of the experiment. A matching problem is carried out, where the fields in regions inside (I), in between (II), and outside (III) the inner and outer wall are solved. From Eq. (5), these field structures are

$$I : B_r(r,\theta) = \Re\left[(A_0 - \tilde{b}r^{-2})e^{-i\theta}\right],$$

$$II : B_r(r,\theta) = \Re\left[(A_1 - A_2 r^{-2})e^{-i\theta}\right],$$

$$III : B_r(r,\theta) = \Re\left[(-A_3)r^{-2}e^{-i\theta}\right],$$

where the B_θ component can be obtained from Eq. (5) for each region. A_n are complex coefficients, and a fluctuating mode source $\tilde{b}$ (T m^2) is the non-homogeneous part of the equation. Matching across the thin walls at r_a and r_b is accomplished using the well known thin-wall jump conditions obtained by integration of the induction equation across the wall at r_w,[23]

$$B_r\big|_{r=r_w^-}^{r=r_w^+} = 0,$$

$$B_\theta\big|_{r=r_w^-}^{r=r_w^+} = -\Omega_w \tau_w B_r.$$

As $r_w/\delta_w \approx 100$ for both walls, the thin-wall approximation is valid for a wide range of ω in the experiment. Applying these conditions at r_a and r_b, a matrix equation is formed for the unknown coefficients

$$\begin{bmatrix} r_a^2 & -r_a^2 & 1 & 0 \\ -r_a^2 & (1+iR_a)r_a^2 & (1-iR_a) & 0 \\ 0 & r_b^2 & -1 & 1 \\ 0 & r_b^2 & 1 & (iR_b-1) \end{bmatrix} \begin{bmatrix} A_0 \\ A_1 \\ A_2 \\ A_3 \end{bmatrix}$$
$$= \begin{bmatrix} \tilde{b} \\ \tilde{b} \\ 0 \\ 0 \end{bmatrix},$$

where $R_a \equiv \Omega_a \tau_a$ and $R_b \equiv \Omega_b \tau_b$. Inverting this matrix yields a unique solution for A_0, which upon substitution of $\{A_0, \tilde{b}\}$ for $\{A_j, A_k\}$ in Eq. (6) yields Γ_{EM} for the differentially rotating two-wall system,

$$\Gamma_{EM} = -4\left(\frac{\tilde{b}^2 \pi L}{r_a^2 \mu_0}\right) \frac{R_a R_b^2 \alpha^2 + 4(R_a + R_b(\alpha+1))}{(4 + R_a R_b \alpha)^2 + 4(R_a + R_b)^2}, \tag{7}$$

which was first given in Eq. (3). The coefficient A_{EM} is thus identified to be $A_{EM} \equiv 4\left(\frac{\tilde{b}^2 \pi L}{r_a^2 \mu_0}\right)$ and is $\mathcal{O}(10^{-2})$ (N m) in the experiment. Equation (7) is able to capture any combination of mode, inner wall, and outer wall rotation by suitable selection of Ω_a and Ω_b.

1. Properties of two-wall electromagnetic torque

The general double-wall torque of Eq. (7) can be easily transformed to a single-wall torque by letting $R_b \to 0$. In this limit, Eq. (7) becomes

$$\Gamma_{EM} = -\left(\frac{\tilde{b}^2 \pi L}{r_a^2 \mu_0}\right) \frac{\omega\tau}{1 + \left(\frac{\omega\tau}{2}\right)^2},$$

which is a well known relation derived elsewhere.[13,14,30,32] The change in Γ_{EM} as the gap between walls (α in Eq. (7)) is
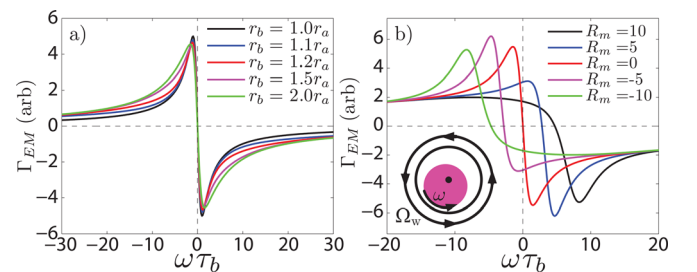

FIG. 2. (a) Wall-induced electromagnetic torque (Γ_{EM}) plotted vs. plasma rotation normalized to the wall time ($\omega\tau_b$) for a variety of inter-wall spacings for equal τ_w walls ($\tau_a = \tau_b$). (b) Modifications to Γ_{EM} for co- and counter-rotation for a variety wall speeds (R_m) utilizing experimental values for $\tau_a, \tau_b = 2\tau_a, r_a$, and $r_b = 1.2r_a$. $\hat{R}_m$ is set by the direction of the natural frequency (Ω_0).

increased, shown in Fig. 2(a), with $\tau_a = \tau_b$ for simplicity (experimentally, $\tau_b = 2\tau_a$). For wall spacings beyond $r_b = 2.0r_a$, little change is seen in Γ_{EM}, indicating the weak coupling limit has been reached. It is found that for the wall spacing corresponding to the experiment ($r_b = 1.2r_a$), the single-wall model is a good approximation at low frequencies but becomes inaccurate at higher frequencies. This can be explained by noting that as $\omega\tau_b \gg 1$, only the inner wall participates as little flux penetrates to the outer wall, so $\Gamma_{EM} \propto (\omega\tau_a)^{-1}$. In general, this is larger than the zero-gap limit where both walls participate, yielding a larger τ and smaller Γ_{EM}. Generally, the ith element (with wall time τ_i) of multi-conductor systems can significantly increase Γ_{EM} in a local region around $\omega\tau_i \approx 1$, as in with discrete tiles lining a vacuum vessel.[31]

The experimentally relevant effect of outer wall rotation on Γ_{EM} is explored by setting $\Omega_a = \omega$ and $\Omega_b = \omega - \Omega_w$. The result is shown in Fig. 2(b), where now $R_m \equiv \Omega_w\tau_b$. While rotation of the single-wall model would rigidly Doppler-shift the curves of Fig. 2(b), differential rotation is found to both Doppler-shift the curves and asymmetrically alter their shape. Co-rotation ($\hat{\Omega}_w = \hat{\omega}$) yields a larger peak in Γ_{EM} at the Doppler-shifted frequency. Conversely, counter-rotation ($\hat{\Omega}_w = -\hat{\omega}$) weakens the peak in Γ_{EM}, until eventually no non-monotonic behavior is seen. As $R_m \mapsto \infty$, the shielding effect becomes dominant and Γ_{EM} is reduced for all frequencies, with only the static inner wall participating weakly. The consequences of differential wall rotation on mode-locking will be discussed in Sec. II E.

B. Derivation of error field torque

Derivation of the torque due to the static error field (Γ_{ext}) is similar to that of the mode-wall electromagnetic torque, where now terms that scale like $\vec{B}_{\text{ext}}\tilde{B}$ are considered in Eq. (2). Using similar arguments as Eqs. (4)–(6), the torque from the static error field is found to be

$$\Gamma_{\text{ext}} = \frac{2Lr_a^2}{\mu_0} \int_0^{2\pi} \vec{B}_{\text{ext},\theta}\tilde{B}_r \exp(-i\phi)d\theta, \quad (8)$$

where no cycle-averaging is carried out. Due to the $\exp(-i\phi)$ and $\exp(-i\theta)$ dependence, the cross-power is of a different form and the torque is found to be

$$\Gamma_{\text{ext}} = 2\left(\frac{L\pi}{\mu_0}\right)B_{\text{ext}}\tilde{b}\sin\phi, \quad (9)$$

where ϕ ($\equiv \int_0^t \omega(t')dt' + \phi_0$) is the complementary angle between $\vec{B}_{\text{ext}}$ and $\tilde{B}$. Thus, A_{ext} is identified in Eq. (3) as $A_{\text{ext}} \equiv 2B_{\text{ext}}\tilde{b}\left(\frac{\pi L}{\mu_0}\right)$ and is $\mathcal{O}(10^{-3})$ (N m) in the experiment. A similar term is present in other treatments[13,32] though as no net torque is generated by Γ_{ext} over a rotation in ϕ, it is often neglected.

As $\vec{B}_{\text{ext}}$ is applied from external conductors, it is also a function of wall rotation. Rotation shields $\vec{B}_{\text{ext}}$ such that $|\vec{B}_{\text{applied}}|/|\vec{B}_{\text{ext}}| = \sqrt{1 + R_m^2/4}$, which can be obtained from solving a matching problem similar to that of Sec. II A.

However, this effect is purposely excluded from Eq. (9) as it is experimentally compensated by applying more current to the error field coil as wall rotation increases.

C. Estimation of phenomenological restoring torque

In order for the torque balance relation of Eq. (2) to capture the mode-locking phenomenology of the experiment, a restoring torque to an offset frequency is required. Most simply, this torque takes the linear form of $\Gamma_{\text{res}} = A_{\text{res}}(\Omega_0 - \omega)$, though higher order dependencies on ω could also yield bifurcations. In this section, it is shown that Γ_{res} could arise from electromagnetic torques forcing the plasma to its "natural" E × B frequency, $\Omega_{\text{E}\times\text{B}}$. Potential gradients, and thus electric fields and E × B flows (shown in Fig. 3), are present in the device due to the large axial bias voltages applied to drive I_p in the relatively cold and resistive plasma. The calculated E × B flow profile is complex, with strong flows near the cathode and vanishing flows near the anode due to the equipotential at the highly conducting anode surface. Radially, the flow profile is well described by the rigid-rotor approximation within the core, though this approximation becomes less accurate at the edge. The rigid-rotor approximation, however, is not able to capture the effects of the axial shear present in the device. How a global mode frequency ω is selected from the sheared rotation profile is also not fully understood.[33] To estimate the restoring torque, the plasma rotation ω is allowed to deviate by δ_ω from Ω_{ExB}, such that $\omega \equiv \Omega_{\text{E}\times\text{B}} + \delta_\omega$. Upon insertion of $V_\theta = r\omega$ into the radial resistive Ohm's law, $E_r + V_\theta B_z = \eta_\perp J_r$ (where $\eta_\perp$ is the cross-field resistivity and $V_z = 0$), E_r cancels $r\Omega_{\text{E}\times\text{B}}$,
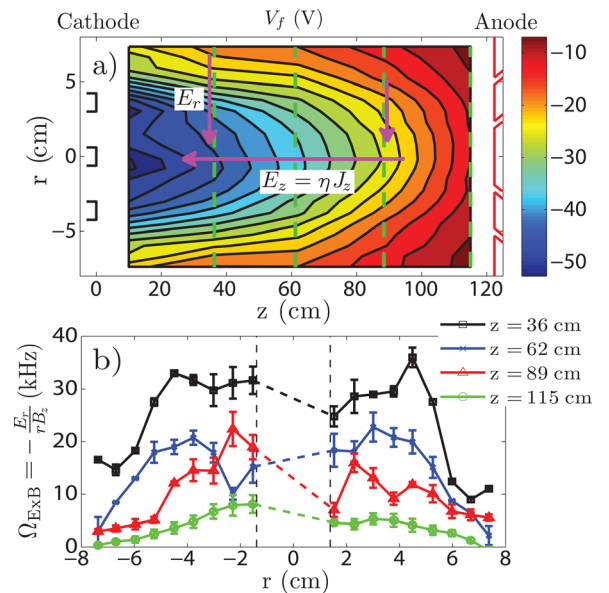

FIG. 3. (a) Floating potential (V_f) measured as a function of radius at different axial locations. (b) Calculated E × B rotation profiles ($\Omega_{\text{E}\times\text{B}}$) from (a). Measurements are made with a single-tip sweeping Langmuir probe using shot-to-shot reproducibility. Other probe measurements[29] (not shown) indicate negligible radial current and uniform T_e, justifying equating gradients in V_f with E_r. Values at small r are skipped to avoid numerical singularities. Measurements are from plasma that yielded a mode at $\omega \approx 12$ kHz, faster than the $\omega \approx 3$ kHz typical of this study.

and it is found that $J_r = \frac{rB_z}{\eta_\perp}(\omega - \Omega_{E\times B})$. Taking only the axisymmetric contribution to Eq. (2),

$$\Gamma_{\text{res}} = \hat{z} \cdot \int_{\mathcal{V}} r \times (\vec{J}_0 \times \vec{B}_0) d\mathcal{V} = -L \int_0^{2\pi} d\theta \int_0^{r_p} r^2 J_r B_z dr$$
$$= \frac{\pi}{2} \frac{L B_z^2 r_p^4}{\eta_\perp} (\Omega_{E\times B} - \omega), \tag{10}$$

where r_p, L are the plasma radius and length, B_z is the (constant) guide field, and $B_r = 0$. From Eq. (10), $A_{\text{res}} \equiv \frac{\pi}{2} \frac{L B_z^2 r_p^4}{\eta_\perp}$ and $\Omega_0 \equiv \Omega_{E\times B}$ are identified. For experimental parameters, $A_{\text{res}} \approx \mathcal{O}(10^{-5})$ (Nm s/rad), and $\Omega_0 \approx \mathcal{O}(10^4)$ (rad/s). In Sec. VI, it will be shown that this estimate is within an order of magnitude of experimental measurements, which is encouraging considering the rudimentary arguments used to arrive at Eq. (10). Note that more complete versions of Ohm's law could be used with a suitable redefinition of $\delta\omega$ and $\Omega_{E\times B}$.

D. Wall-locking: Bifurcations in torque balance

Solutions of Eq. (3) are explored first with $R_m = 0$ and $\Gamma_{\text{ext}} = 0$ for simplicity, with results similar to earlier treatments despite the inclusion of a second wall.[12–14,32] Figs. 4(a)–4(d) illustrates the various regimes of Eq. (3) possible when scanning Ω_0 while holding A_{EM} and A_{ext} fixed. As will be discussed in Sec. III, this is the experimentally relevant treatment. For large Ω_0, shown in Fig. 4(a), there is only one root at $\omega \approx \Omega_0$ which is dynamically stable and is termed the fast branch. As Ω_0 is decreased, as in Fig. 4(b), 3 roots are found—the fast branch, a new stable slow branch, and an unstable branch. Lowering Ω_0 further the locking bifurcation point is reached, shown in Fig. 4(c), where the fast and unstable branches merge. Below this critical value of Ω_0, only the slow branch remains, as shown in Fig. 4(d). Figure 4(e) summarizes the solutions of Eq. (3). Locking bifurcations thus occur when Ω_0 is lowered, past the bifurcation point and the mode transitions discontinuously from $\omega \approx \omega_{\text{lock}} \to 0$ on an inertial time-scale, which is sub-ms for the experiment. Another possible bifurcation is mode unlocking, in which raising Ω_0 past the unlocking threshold transitions, the mode from the slow to fast branch. As expected, hysteresis is present.

The effect of Γ_{ext} on the picture of Fig. 4 is only important near the bifurcation point as over a cycle there is no net torque and the roots of Eq. (3) are not modified. Within each cycle, Ω_0 effectively oscillates at $\approx \omega$ such that $\Omega_0(t) = \Omega_0 + \tilde{\Omega}_0 \sin\phi$, where $\tilde{\Omega}_0 \equiv A_{\text{ext}}/A_{\text{res}}$, as shown in Fig. 4(e). Near the bifurcation, this excursion in Ω_0 can induce a bifurcation at $\Omega_0 = \Omega_{0,\text{lock}} + \tilde{\Omega}_0$, which would be observed as a lock at higher frequency than predicted in the absence of an error field. In Secs. III and IV, it will be shown that this correction is necessary to interpret the observed data.

E. Bifurcations with differential rotation

The bifurcations of Eq. (3) are now explored with the inclusion of differential wall rotation. Fig. 5(a) illustrates the modification of the roots of Eq. (3) by wall rotation. The fast
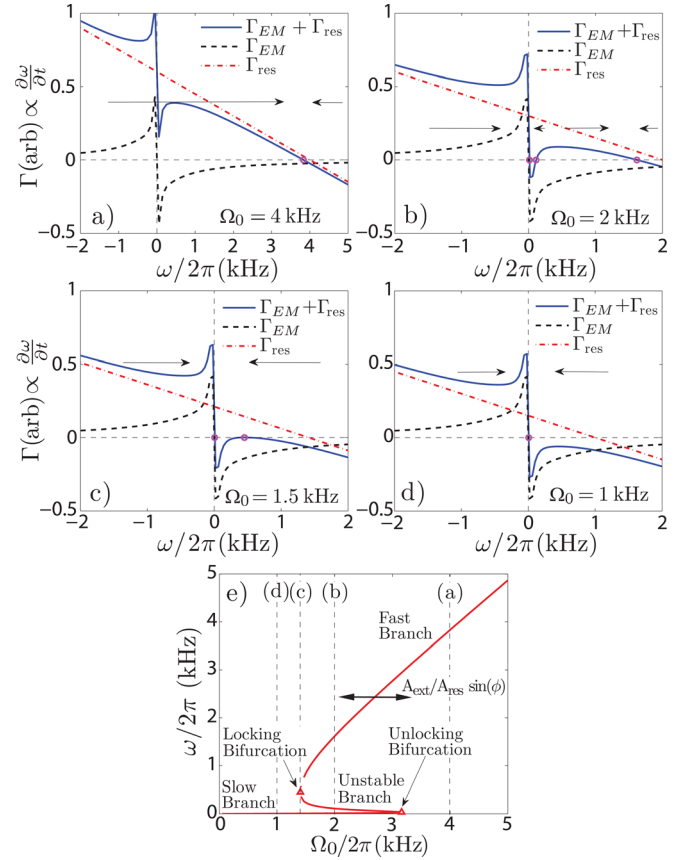
FIG. 4. (a)-(d) Net electromagnetic torque (Γ) as a function of plasma rotation (ω) decomposed into electromagnetic (Γ_{EM}) and restoring (Γ_{res}) contributions for various values of natural frequency (Ω_0). Other variables in Eq. (3) are held constant. Arrows in (a)-(d) indicate the direction of net torque and thus point to the stable solutions. (e) This bifurcation diagram is made by plotting the torque balance equilibrium points (solutions of Eq. (3)) while varying Ω_0, illustrating the locking and unlocking bifurcation points.

branch is largely unaffected by rotation, while the slow branch is shifted to $\omega \approx \Omega_w/2$. The unstable branch, and thus the bifurcations, are strongly affected by rotation as summarized in Fig. 5(b). The locking bifurcation at ω_{lock} is monotonically Doppler shifted by rotation, while the natural frequency required to lock the mode ($\Omega_{0,\text{lock}}$) is insensitive to wall rotation. The unlocking bifurcation at ω_{unlock} is also Doppler shifted, though a very dramatic effect on $\Omega_{0,\text{unlock}}$ is found.
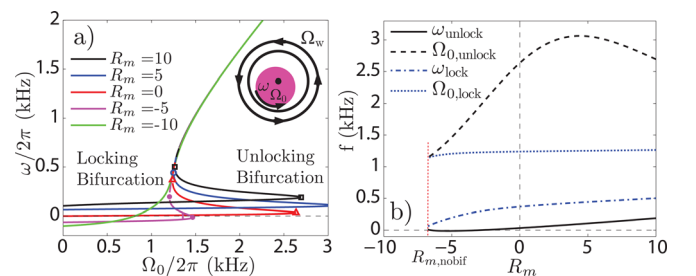
FIG. 5. (a) Bifurcation diagram illustrating torque balance equilibrium points (solutions of Eq. (3)) as Ω_0 is varied for various values of differential wall rotation (R_m). (b) Dependence of the locking and unlocking bifurcation frequencies ($\omega_{\text{lock}}, \omega_{\text{unlock}}$) and natural frequencies ($\Omega_{0,\text{lock}}, \Omega_{0,\text{unlock}}$) as R_m is varied. Beyond $R_{m,\text{nobif}}$ the bifurcation is lost.

For co-rotation ($R_m > 0$), $\Omega_{0,\text{unlock}}$ is found to increase, thus requiring more torque to unlock a locked mode, until at fast rotation shielding weakens this effect. In contrast, counter-rotation ($R_m < 0$) dramatically decreases $\Omega_{0,\text{unlock}}$ until both bifurcations are completely lost at $R_{m,\text{nobif}}$. Thus, for fast counter-rotation, mode-locking is not predicted to occur and a mode could transition unimpeded from slow to fast rotations. Wall counter-rotation above $R_{m,\text{nobif}}$ has thus removed the ability of the mode to lock to any wall.

The locking asymmetry in R_m reverses as $\Omega_0 \mapsto -\Omega_0$, justifying the definition of co- and counter-rotation by Ω_0. Were $\Omega_0 = 0$, there would be no asymmetry, though the only solution to Eq. (3) would be the locked branch at $\omega \approx \Omega_w/2$, precluding bifurcations. Lastly, as the rotating wall is a realization of a perfect active control system with a single value of complex gain,[24] active control of MHD modes would alter the torque balance in an equivalent manner. Thus, in addition to directly reducing the mode amplitude, active control may also stabilize modes by altering their unlocking bifurcations.

III. STATIC WALL MODE-LOCKING

The model developed in Sec. II will be shown to capture the effects of both $m = 0$ and $m = 1$ error fields with the rotating wall left stationary for simplicity. All static error fields are applied as a part of the vacuum field configuration well prior to plasma formation and flux-loop integration and thus are not directly detected.

A. Slowing of plasma rotation by guide field ripple

The application of axially localized, steady-state $m = 0$ fields (guide field ripple, $\tilde{B}_z$) is found to have a strong effect on the observed mode frequency ω. This is shown in Fig. 6(a), where other plasma parameters are held constant. At low $\tilde{B}_z$, the mode is always in the fast branch and $\Omega_0 \approx \omega$. As a characteristic fast slow-down followed by modest increase in ω is typical of all discharges in the device, as shown in Fig. 6(b), $\Omega_0(t)$ will be fit to the following analytic form

$$\Omega_0(t) = a_1 + a_2\left(1 - \exp\left(-\frac{t}{a_3}\right)\right) + a_4 \exp\left(\frac{t}{a_5}\right), \quad (11)$$

where a_n are positive definite coefficients. Specifically, $a_n \approx [1, 2, 2.5, 2.01, 2.5]$ [kHz, kHz, ms, kHz, ms], respectively, is found to well match the data for the discharges of this study. As $\Omega_0(t)$ is an input to the model, its self-consistent evolution is beyond the scope of this paper. Measurements of A_{ext} and A_{EM} (not shown) are found to be remarkably constant in time for these discharges, indicating that the rotating RWM amplitude ($\tilde{B}$) is constant and stabilized by plasma rotation. As the flux-loops are located outside the static wall, all amplitude variations in Fig. 6(a) are due to the shielding effect of the wall on the measurement of $\tilde{B}$. The interpretation of field ripple in terms of the bifurcation picture of Sec. II D is shown in Fig. 6(c) for constant A_{res} and measured A_{ext}, A_{EM}. Increasing $\tilde{B}_z$ causes Ω_0 to plunge further towards the bifurcation point as a function of time. While the largest ripple case did not lock, the very low
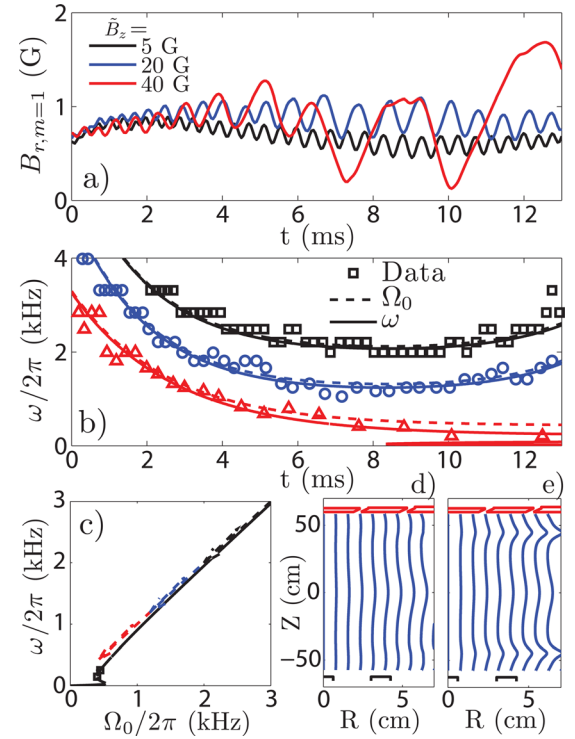

FIG. 6. (a) Time-trace of radial magnetic field ($B_{r,m=1}$) as guide field ripple ($\tilde{B}_z$) is increased. (b) Measurements of mode frequency (ω) for the discharges of (a). For Figs. 6–12, $\Omega_0(t)$ is fit (according to Eqs. (3) and (11)) such that $\omega(t)$ matches the data, holding other parameters in Eq. (3) constant. (c) Bifurcation diagram (roots of Eq. (3)) calculated using the data from the fits of (b). (d)-(e) The calculated alteration of the guide field by the $\tilde{B}_z$ coil is shown, where panel (d) is for $\tilde{B}_z = 5$ G while panel (e) is for $\tilde{B}_z = 40$ G. The top, bottom outlines in (d) and (e) indicate the position of the segmented anode and plasma guns, respectively. $t = 0$ is when the bias voltage to drive I_p is applied.

ω and continually slowing time-dependence indicate it neared the locking threshold. Figures 6(d) and 6(e) illustrates the modification of the vacuum fieldlines by $\tilde{B}_z$. While the ripple coils are axially localized, they have a global effect on the mode frequency. It is speculated that $\tilde{B}_z$ is hollowing the $J_z(r)$ profile, whose radial gradient is thought to set E_r and thus Ω_0, as discussed in Sec. II C.

B. Mode-locking by vertical error fields

Increasing the static, vertical ($m = 1$, $k_z = 0$) error field ($\equiv \vec{B}_{\text{ext}}$) is found to lock the RWM at progressively higher frequencies, giving rise to three distinct regimes as shown in Fig. 7. First, at low $\vec{B}_{\text{ext}}$, the RWM does not lock for the duration of the discharge and is termed as a rotating RWM. At intermediate $\vec{B}_{\text{ext}}$, the RWM initially rotates and locks during the discharge. As indicated in Fig. 7(b), for the $B_{\text{ext}} = 2$ (3) G case, the mode frequency abruptly jumps to zero at $t \approx 2$ (5) ms. This is termed as a locked RWM. For large $\vec{B}_{\text{ext}}$, no oscillations are seen and the mode is termed born-locked. Like $\tilde{B}_z$, $\vec{B}_{\text{ext}}$ is applied prior to plasma formation and flux-loop integration and, thus, is not directly measured. However, $\vec{B}_{\text{ext}}$ forces the resulting equilibrium to be centered off-axis, thus causing an $m = 1$ component to the equilibrium field ($\equiv \vec{B}_{\text{eq}}$) that is detected. $\vec{B}_{\text{eq}}$ can thus be thought of as the plasma response and is a proxy for $\vec{B}_{\text{ext}}$.
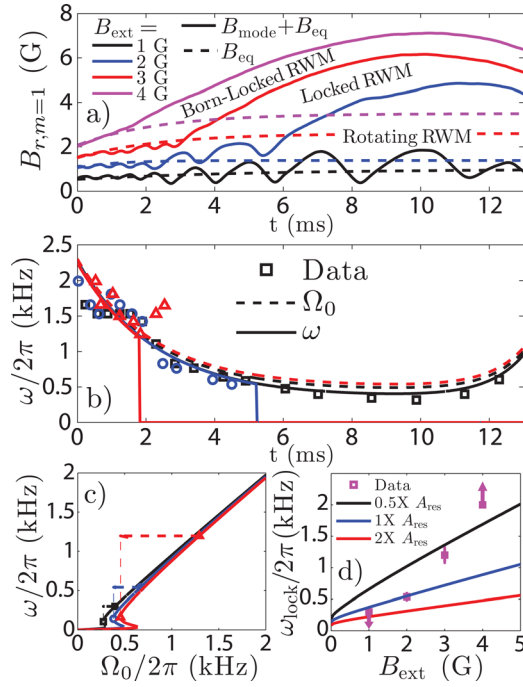
FIG. 7. (a) Time-traces of radial magnetic field ($B_{r,m=1}$) as $m = 1$ error field (B_{ext}) is increased, yielding mode locking. (b) Mode rotation (ω) and resultant fits to the model of Eqs. (3) and (11). (c) Bifurcation diagrams (solutions of Eq. (3)) using the fit parameters of (b). (d) Expected locking frequencies (ω_{lock}) as B_{ext} is increased and comparison to the data. Arrows in (d) indicate that no locking bifurcation was observed, thus ω_{lock} must be in the direction shown.

Increasing $\vec{B}_{ext}$ both increases $\vec{B}_{eq}$ and modifies ω_{lock}, as shown in Fig. 7(b). Using the model of Eq. (3) with measurements of the ω_{lock}, A_{ext}, and A_{EM} as inputs, curves of the form of Fig. 7(c) are generated. Ω_0 decreases throughout the discharge until the modified locking condition $\Omega_0 = \Omega_{0,lock} + A_{ext}/A_{res}$ is reached (as discussed in Sec. II D). An intermediate amount of $\tilde{B}_z$ is also applied to bring Ω_0 closer to the locking threshold, as suggested by Fig. 6. At fast ω, $\vec{B}_{ext}$ is observed to have no effect whatsoever on the $\omega(t)$ trace, confirming that $\vec{B}_{ext}$ does not modify the torque balance when integrated over a cycle. The model of Sec. II predicts a roughly linear increase in ω_{lock} with increasing $\vec{B}_{ext}$ if all other parameters are held constant. However, as shown in Fig. 7(d), the observed increase in ω_{lock} is larger than the prediction. Allowing A_{res} to vary as $\vec{B}_{ext}$ is increased yields better agreement, indicating that $\vec{B}_{ext}$ may be altering the torque balance beyond simply modifying the static error field torque. Nonetheless, the model of Eq. (3) captures the trend in ω_{lock} and captures the discontinuous nature of the locking transition. The fact that locking occurs at the same phase (ϕ) also reinforces the idea that Γ_{ext} is responsible for locking.

C. Near-threshold effects

1. Sensitivity to input conditions

The sensitivity of the locking bifurcation to input conditions is shown in Fig. 8, which compares two successive discharges where no change was made to the experimental control parameters. Very different outcomes were obtained as the first discharge locked while the second did not, as
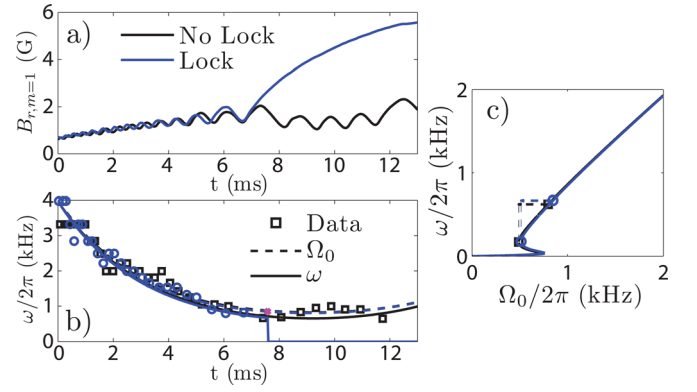

FIG. 8. (a) Radial magnetic field ($B_{r,m=1}$) time-traces for two sequential discharges. (b) Mode rotation (ω) and fits to Eqs. (3) and (11) for the discharges in (a). (c) Bifurcation diagram (solutions of Eq. (3)) using fits from (b).

would be expected of the behavior of Eq. (3) near the locking threshold. Holding $\Omega_0(t), A_{EM}, A_{ext}$ constant and allowing A_{res} to vary by 8% is sufficient to differentiate between a discharge that is predicted to lock and one that is not, further reinforced by the small difference in the solutions to Eq. (3) shown in Fig. 8(c). Variations of A_{res} at this level are thus thought to define the level of repeatability attainable in the experiment.

2. Non-uniform rotation

As discussed in Sec. II D, the effect of Γ_{ext} is to oscillate the effective Ω_0 such that $\Omega_0(t) = \Omega_0 + A_{ext}/A_{res} \sin\phi$. Letting $\phi \equiv \int_0^t \omega(t)dt \approx \langle\omega\rangle t$ shows that this should in principle result in an oscillation of ω at $\approx \langle\omega\rangle$ as well, such that $\omega(t) \approx \langle\omega\rangle + \tilde{\omega}\sin\langle\omega\rangle t$, where $\tilde{\omega}$ depends on the nature of the other torques in the system. At low ω, the deviation from $\langle\omega\rangle$ throughout a cycle can be observed in the experiment. Figure 9 illustrates a sample discharge where a long oscillation prior to locking is observed. Removing the approximate error field by a linear fit isolates the oscillation. It is clear that the oscillation is inconsistent with a single, constant
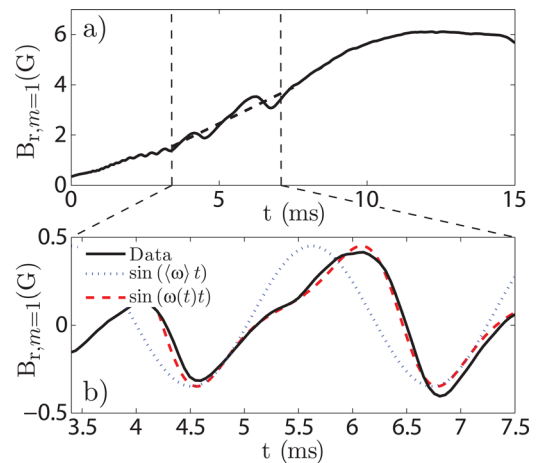

FIG. 9. (a) Radial magnetic field ($B_{r,m=1}$) for a discharge where locking occurred (at $t \approx 7$ ms) after a longer final oscillation. (b) Enlargement of this final oscillation with fits to a single frequency model ($\sin(\omega t)$) and one in which $\omega(t) = \langle\omega\rangle + \tilde{\omega}\sin\langle\omega\rangle t$.

$\langle\omega\rangle$. Introducing $\tilde{\omega}$ into the form of $\omega(t)$ yields much better agreement, with a curve characteristic of nested sinusoids observed. The best fit is found for $\tilde{\omega} = 0.7\langle\omega\rangle$, which supports the significant role of Γ_{ext} in the observed mode-locking. The exact form of the curve also depends sensitively on the initial conditions (ω_0 and ϕ_0), with different shapes seen in different discharges.

3. Hysteresis in mode-unlocking

The model of Sec. II also predicts a second bifurcation when a locked mode's natural frequency (Ω_0) exceeds a critical value, thus allowing the mode to discontinuously unlock. The discharge shown in Fig. 10 exhibits mode-locking occurring at $t \approx 5$ ms followed by mode-unlocking at $t \approx 10$ ms. The frequency immediately after the mode-unlocking is clearly larger than that immediately before the lock, thus illustrating hysteresis. Figure 10(c) illustrates the discharge evolution in terms of the bifurcation diagram of Sec. II D, showing both the locking and unlocking transitions. For simplicity, this is done assuming constant A_{res}, A_{ext}, and A_{EM} before and after locking, which may account for the discrepancy in the predicted frequency after mode-unlocking. It should be noted that mode-unlocking is a rare phenomenon in the experiment, with locked modes almost always remaining locked throughout the discharge. This is thought to be because Ω_0 does not normally reach a sufficiently large value at the end of the discharge.

IV. MODE-LOCKING WITH DIFFERENTIAL WALL ROTATION

Mode-locking in discharges with differential wall rotation is compared to the predictions of Sec. II E, with wall rotation found to affect mode-locking asymmetrically. As shown in Fig. 5, mode-locking is expected to occur at higher frequency for co-rotation ($R_m > 0$) and lower frequency for counter-rotation ($R_m < 0$). For all discharges in this section, $\vec{B}_{ext}$ is held approximately constant by applying more error field current as R_m is increased to overcome the shielding by the rotating wall.
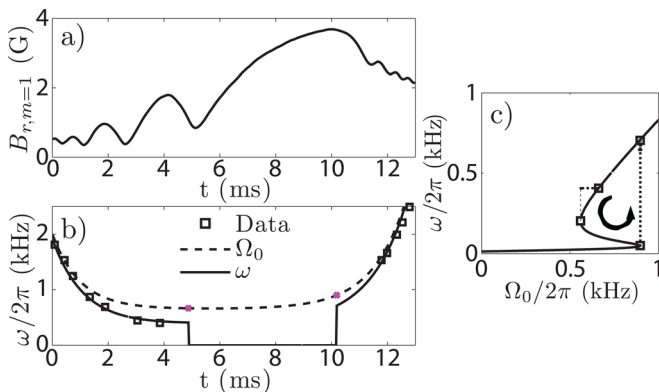
The co-rotation case is shown in Fig. 11, with locking observed at higher ω as wall rotation is increased. Figure 11(c) illustrates the solutions to Eq. (3) with increasing wall rotation. To better match the data, A_{res} has been allowed to vary, though $\Omega_0(t)$ has been held nearly constant. As shown in Fig. 11(d), the observed increases in ω_{lock} are greater than that expected by the constant A_{res} model, indicating that wall rotation may be affecting other parameters in the simple model of Eq. (3), though the data is contained within a narrow band of A_{res}.

Inhibited locking by counter-rotation is shown in Fig. 12. For only these discharges, I_p has been lowered from 6.0 to 5.3 kA in order to alter ω_{lock} and lock at $R_m = 0$ with low $\vec{B}_{ext}$. Note the modification of ω_{lock} as plasma parameters are varied is beyond the scope of this study. While at early time, $\Omega_0(t)$ is constant between discharges, the $R_m = 0$ case slows and locks while the $R_m < 0$ cases continue unlocked throughout the discharge. Figure 12(c) shows the modifications to the solutions of Eq. (3) for experimental parameters, and Fig. 12(d) summarizes the results by noting the change in ω_{lock} as R_m is varied.

V. STABILIZATION OF LOCKED MODES BY WALL ROTATION

Attention is now turned to the interaction of locked modes with the rotating conducting wall. Locked modes must be used as $\omega \approx \mathcal{O}(\Omega_w)$ is necessary for wall rotation to significantly affect the RWM, whereas for rotating RWMs, $\omega \gg \Omega_w$. Unlike Secs. I–IV, comparisons here will be made to an analytic model for RWM stability in a screw pinch surrounded by thin walls, described in Ref. 23. This ideal MHD
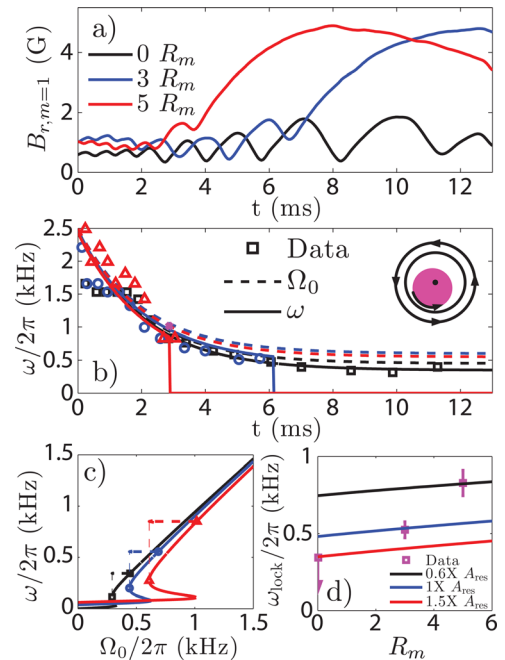
FIG. 11. (a) Radial magnetic field ($B_{r,m=1}$) traces illustrating mode-locking at higher frequency due to wall co-rotation ($R_m > 0$). (b) Mode rotation (ω) traces and corresponding fits to Eqs. (3) and (11). (c) Bifurcation diagram (solutions of Eq. (3)) for fit parameters from (b). (d) Comparison of theoretical and experimental locking bifurcation frequency (ω_{lock}) as R_m is varied for a range of values of A_{res}.

FIG. 10. (a) Time-trace of radial magnetic field ($B_{r,m=1}$) for a discharge illustrating mode-unlocking. (b) Mode rotation (ω) and fits to Eqs. (3) and (11) for the same discharge. (c) Bifurcation diagram (solutions of Eq. (3)) using fits from (b), illustrating mode-locking and mode-unlocking bifurcations at constant A_{res}, A_{ext}, and A_{EM}.
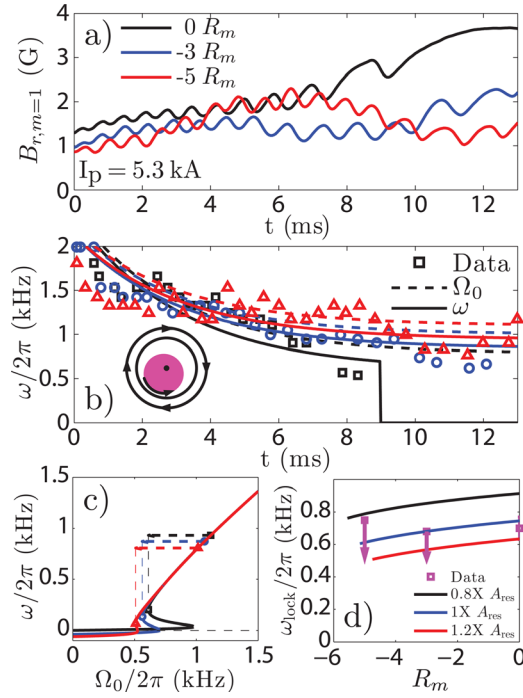
FIG. 12. (a) Radial magnetic field ($B_{r,m=1}$) traces illustrating mode-locking at lower frequency due to wall counter-rotation ($R_m < 0$). (b) Mode rotation (ω) traces and corresponding fits to Eqs. (3) and (11). (c) Bifurcation diagram (solutions of Eq. (3)) for fit parameters from (b). (d) Comparison of theoretical and experimental locking bifurcation frequency (ω_{lock}) as R_m is varied for a range of A_{res}. As a lock is only observed for $R_m = 0$, only the upper bound of ω_{lock} is known.

model takes the plasma to be force-free, with zero flow and with a top-hat current profile. Stability is calculated by solving the eigenvalue problem for a given plasma radius (r_p) and current (I_p). Here, the parameter of interest to RWM stability is the safety factor $q(r)$,

$$q(r) = \frac{4\pi^2 r^2 B_z}{\mu_0 I_p(r) L},$$ (12)

where L is the device length. As the model current profile is top-hat like, a well-defined r_p exists and stability is uniquely determined by $q(r_p)$. $q(r)$ is constant for $r < r_p$, thus the effect of magnetic shear is not included. With no rotation, instability to the RWM is found at $q(r_p) < 1$, matching the Kruskal-Shafranov limit.[34,35] When wall rotation is introduced, the plasma can be stable at $q(r_p) < 1$ and a prediction for the required critical rotation is given, using the notation of this paper,

$$R_{m,crit}^2 = \frac{4\alpha_a(1-q)}{(\alpha_a - \alpha_b)(q-1+\alpha_b)} \left[1 + \left(\frac{\tau_b}{\tau_a}\right) \frac{q-1+\alpha_b}{q-1+\alpha_a}\right]^2,$$ (13)

where $\alpha_a \equiv (r_p/r_a)^2$, $\alpha_b \equiv (r_p/r_b)^2$, and $q \equiv q(r_p)$. Coupling to the rotating wall, and thus stabilization, is found to be more effective as r_p approaches r_a. Experimentally, a three-part radially segmented anode provides a coarse measurement of $q(r)$ at $r = 2, 5, 8\,\text{cm}$ as the current within the outer diameter of each anode ring ($I_p(r)$) is known.

A. Growth rate reduction and locked-mode rotation

Holding the error field ($\vec{B}_{ext}$) and $m=1$ equilibrium plasma response ($\vec{B}_{eq}$) constant in a regime where the RWM locks during the discharge lifetime allows the stabilizing effect of the wall to be clearly demonstrated, as shown in Fig. 13. Though mode-locking is a non-linear phenomenon and, thus, the predictions of Ref. 23 are strictly speaking invalid, it is found that increasing $|R_m|$ both reduces the growth rate of $\vec{B}_{mode}$ from the $\vec{B}_{eq}$ baseline and imparts rotation (ω) to the locked mode. Qualitatively, these results are in agreement.

The displayed traces of $\vec{B}_{eq}$ in Fig. 13 are experimentally obtained by minimizing $\tilde{B}_z$ such that the mode rotates very quickly (kHz scale, irrespective of $\vec{B}_{ext}$) as suggested by Fig. 6. $\vec{B}_{mode}$ is thus shielded from the flux-loop array by the conducting walls and only $\vec{B}_{eq}$ is measured. This technique is imperfect, as can be noted from both the slight deviation of $\vec{B}_{eq}$ from the mean of $\vec{B}_{mode} + \vec{B}_{eq}$ from 0 to 4 ms, as well as the difference between $\vec{B}_{eq}$ from $R_m = 0$ to $R_m = -5$. The evolution of $\vec{B}_{eq}$ itself can thus also be slightly influenced by wall rotation, a topic which is beyond the scope of this paper.

Hodograms clearly illustrate the discontinuous behavior at the locking bifurcation, which occurs just after the final circular motion in Fig. 13(c). Progressively larger locked mode real frequencies (ω) are also observed. This value is found to be consistent with the prediction of $\omega \approx \Omega_w/2$.[23] It is also clear that the $R_m = 0$ locked mode is not exactly at $\omega = 0$, but that a very small residual rotation is present, which can give rise to a Doppler shift in the resultant locked mode rotation when $|R_m| > 0$.[26]

B. Extension of stability window to higher current

Experiments utilizing born-locked modes allow the demonstration that $|R_m| > 0$ operation increases the window of RWM-stable operation, as shown in Fig. 14. Discharges are carried out at constant B_z and $\vec{B}_{ext}$, such that RWM onset is found as I_p is increased [$q(r)$ decreased]. Shot-to-shot reproducibility is used to scan I_p as each data point in Fig. 14 is a separate discharge. Born-locked modes (largest amplitude traces of Fig. 7) are used to avoid confusion between locking thresholds and RWM onset conditions.[11] This is
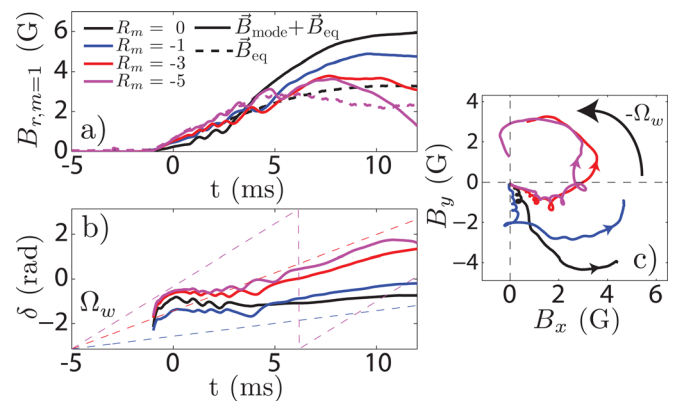

FIG. 13. Time-traces of (a) amplitude ($B_{r,m=1}$), (b) phase (δ), and (c) hodogram (B_x vs B_y) of the radial magnetic field as wall rotation (R_m) is increased, while holding error fields ($\vec{B}_{ext}$ and $\vec{B}_{eq}$) constant. Dotted lines in (b) indicate the rate of wall rotation.
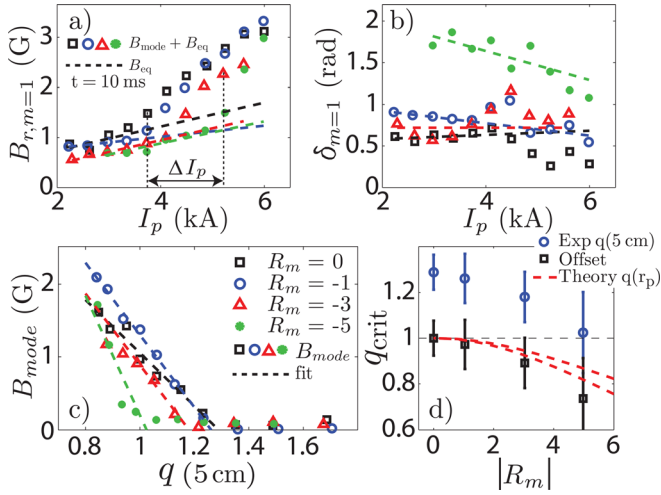
FIG. 14. (a) $B_{r,m=1}$ amplitude diverges from $\vec{B}_{eq}$ at a critical I_p which is raised as R_m increases. (b) Phases of $\vec{B}_{mode} + \vec{B}_{eq}$ also vary as I_p increases. (c) $\vec{B}_{mode}$ amplitude as a function of q as measured by the anode ring at $r = 5$ cm. (d) Comparison of the experimental data and theoretical predictions of the critical q (q_{crit}) for instability. The squares in (d) have been offset such that $q_{crit} = 1$ for $R_m = 0$. Reprinted with permission from Paz-Soldan *et al.*, Phys. Rev. Lett. **107**, 245001 (2011). Copyright © 2011, American Physical Society.

especially important given that wall rotation also alters the locking threshold, as discussed in Sec. IV.

Onset is determined by noting where $\vec{B}_{mode} + \vec{B}_{eq}$ diverges from the $\vec{B}_{eq}$ baseline as I_p is raised, as shown in Figs. 14(a) and 14(b). As $\vec{B}_{ext}$ is not directly measured and $\vec{B}_{eq}$ arises from plasma equilibrium currents, B_{eq} is linear in I_p. A subtraction of a linear fit to $\vec{B}_{eq}$ is carried out to isolate the RWM signature, $\vec{B}_{mode}$. Figure 14(c) illustrates $\vec{B}_{mode}$ amplitude, with higher $|R_m|$ operation yielding mode onset at lower $q(r)$ as measured by the 5 cm radius anode ring. The resultant critical q for RWM onset (q_{crit}) as $|R_m|$ is increased is shown in Fig. 14(d) and compared to the theoretical prediction. Specifically, the experimental q_{crit} is taken from the zero-crossing of the fits in Fig. 14(c) with errors derived from the confidence intervals of this fit. Theoretical curves are directly calculated from Eq. (13) taking $r_p = 6.5, 7.5$ cm (upper, lower curve). Defining a single r_p for the experimental plasma is ambiguous and thus a source of uncertainty. Also note the model q profile is constant for $r < r_p$. The experimental q_{crit} is larger than the theoretical prediction for all R_m, as will be discussed in Sec. VI. Offsetting the experimental data such that $q_{crit} = 1$ when $R_m = 0$, the change in q_{crit} as $|R_m|$ increases ($\equiv \Delta q_{crit}$) is found to be in agreement with theory. Similar agreement is found if the data is scaled rather than offset. It is also found that the stabilizing effect is modest until high R_m is achieved, consistent with the quadratic scaling of Eq. (13).

VI. DISCUSSION

Regarding RWM stabilization, this experiment has shown qualitative agreement with the theory of Ref. 23. Wall rotation has been shown to increase the RWM stability window, decrease the mode growth rate, and impart rotation to the locked RWM. Nonetheless, discrepancies remain. Exponential growth is not observed, likely due to the inherent non-

linearities present in mode-locking phenomena and the presence of locked mode rotation. Further, although Δq_{crit} is found to be in agreement, q_{crit} is measured to be larger in experiment [$q(5 \text{ cm}) = 1.3 \pm 0.1$] than in theory [$q(r_p) = 1.0$]. This disagreement is most likely explained by non-ideal MHD effects neglected in the model used to derive Eq. (13). For example, the flow profile of the locked modes has not been measured and may alter the resultant stability. Resistivity,[36] pressure,[37] magnetic shear,[38] and flow[39] have been included separately in other theoretical treatments of the kink mode, though these studies did not include a rotating conducting wall. The coarseness of the $q(r)$ measurement also introduces uncertainty, as would any axial variation in the current profile.

Several points are raised by the functional equivalence of Eq. (3) to the established torque balance models.[10,12–15] These models are fundamentally layer theories, with ideal MHD violated either at a rational surface or in a thin inertial layer. Some form of dissipation, or violation of ideal MHD, is necessary for the electromagnetic torque to exist,[13] as in ideal MHD $\nabla \cdot \bar{\bar{T}} = \nabla P$ which vanishes over surface integration. In this model, the two main sources of dissipation are resistivity η and viscosity. Resistivity in the wall is explicitly used in the calculation of Γ_{EM} in Eq. (7), while resistivity in the plasma is invoked to approximate Γ_{res} in Eq. (10). Though viscosity does not explicitly appear in this study, the use of the rigid-rotor approximation implies it is the dominant term in setting the rotation profile. Figure 3 supports this in the core of the device, though at the edge this is less clear. It is thus not surprising that electromagnetic body torques are present in the experiment despite their absence in ideal MHD.

The role of the error field ($\vec{B}_{ext}$) in the torque balance model is contained entirely in the Γ_{ext} term of Eq. (3) and $\vec{B}_{ext}$ is shown to exert no net torque over a cycle in ϕ. In the long-cylinder model, the error field is resonant with the mode as $k_z = 0$ for both. Experimentally, however, the cylinder is finite and bounded by highly conducting electrodes, thus requiring at least two $k_z \neq 0$ for the RWM, and more k_z in the presence of magnetic shear.[38] Thus, the error field is not obviously resonant in the experiment. Nonetheless, $\vec{B}_{ext}$ is observed to strongly affect mode-locking phenomenology and alter the locking frequency ω_{lock} as discussed in Sec. III B. It is speculated that either the resonance condition is relaxed by the strong dissipation everywhere in the plasma or some k_z are sufficiently small that they are effectively resonant with $\vec{B}_{ext}$. The relationship between $\tilde{B}$ and $\vec{B}_{ext}$ has also been neglected in this model. This in contrast to the treatment of tearing modes, where $\vec{B}_{ext}$ is responsible for driven reconnection which introduces $\tilde{B}$. However, for the experimental geometry, it is not evident that $\tilde{B}$ would be affected by $\vec{B}_{ext}$, thus justifying their independence in the model.

Each observation of mode-locking in this study has yielded a measurement of A_{res}. An equation to solve for the locking bifurcation point $\{\omega_{lock}, \Omega_{0,lock}\}$ is readily obtained as bifurcation occurs where the discriminant of Eq. (3), written as a polynomial in ω, vanishes. In the aforementioned discharges, $\Gamma_{EM}, \Gamma_{ext}$, and ω_{lock} are experimentally measured by the flux-loop array, giving a unique prediction for A_{res}. For the discharges of this study, measured values of A_{EM}, A_{ext} and calculated values of A_{res} are shown in Table I. Despite the wide

TABLE I. Measured values of A_{EM}, A_{ext} and calculated values of A_{res} from the discharges of this study. Errors are estimated from the deviations between and within discharges.

Description	$\langle A_{res}\rangle * 10^6$	$\langle A_{EM}\rangle * 10^2$	$\langle A_{ext}\rangle * 10^3$
m = 0 fields (Fig. 6)	0.4 ± 0.2	0.5 ± 0.2	0.2 ± 0.1
m = 1 fields (Fig. 7)	1.6 ± 0.7	1.9 ± 0.7	$1-4$
Sensitivity (Fig. 8)	0.5 ± 0.1	1.0 ± 0.3	1.0 ± 0.3
Unlocking (Fig. 10)	1.1 ± 0.5	2.5 ± 0.5	0.7 ± 0.2
Co-ω (Fig. 11)	0.9 ± 0.5	0.6 ± 0.2	0.7 ± 0.2
Counter-ω (Fig. 12)	0.3 ± 0.1	1.3 ± 0.5	1.4 ± 0.4

range of discharges used in each comparison, $A_{res} \approx \mathcal{O}(10^{-6})$ for all cases. This is smaller than the $\mathcal{O}(10^{-5})$ estimate of Sec. II C. This level of disagreement is acceptable as several approximations were used to arrive at Eq. (10), specifically the simplification of the rotation profile of Fig. 3(b) to simple rigid-rotation and the neglect of other terms in the radial Ohm's law. Furthermore, though a possible mechanism has been identified for the restoring torque in Sec. II C, other mechanisms could be occurring in conjunction. Torques from neutral collisions,[40] direct losses,[41] turbulent stresses,[42] or other anomalous torques can generally be lumped into the parametric form of $A_{res}(\Omega_0 - \omega)$ as long as they are linear in ω and, thus, would alter the prediction of Γ_{res}.

ACKNOWLEDGMENTS

[1]C. Paz-Soldan, W. F. Bergerson, M. I. Brookhart, D. A. Hannum, R. Kendrick, G. Fiksel, and C. B. Forest, Rev. Sci. Instrum. **81**, 123503 (2010).

[2]M. S. Chu and M. Okabayashi, Plasma Phys. Controlled Fusion **52**, 123001 (2010).

[3]C. G. Gimblett, Nucl. Fusion **26**, 617 (1986).

[4]E. J. Strait, T. S. Taylor, A. D. Turnbull, J. R. Ferron, L. L. Lao, B. Rice, O. Sauter, S. J. Thompson, and D. Wrblewski, Phys. Rev. Lett. **74**, 2483 (1995).

[5]A. M. Garofalo, A. D. Turnbull, E. J. Strait, M. E. Austin, J. Bialek, M. S. Chu, E. Fredrickson, R. J. La Haye, G. A. Navratil, L. L. Lao, E. A. Laza-

rus, M. Okabayashi, B. W. Rice, S. A. Sabbagh, J. T. Scoville, T. S. Taylor, and M. L. Walker, Phys. Plasmas **6**, 1893 (1999).

[6]E. J. Strait, Phys. Plasmas **1**, 1415 (1994).

[7]A. Bondeson and D. J. Ward, Phys. Rev. Lett. **72**, 2709 (1994).

[8]B. Hu and R. Betti, Phys. Rev. Lett. **93**, 1 (2004).

[9]J. W. Berkery, S. A. Sabbagh, R. Betti, B. Hu, R. E. Bell, S. P. Gerhardt, J. Manickam, and K. Tritz, Phys. Rev. Lett. **104**, 035003 (2010).

[10]R. Fitzpatrick, Phys. Plasmas **9**, 3459 (2002).

[11]A. M. Garofalo, G. L. Jackson, R. J. La Haye, M. Okabayashi, H. Reimerdes, E. J. Strait, J. R. Ferron, R. J. Groebner, Y. In, M. J. Lanctot, G. Matsunaga, G. A. Navratil, W. M. Solomon, H. Takahashi, M. Takechi, and A. D. Turnbull, Nucl. Fusion **47**, 1121 (2007).

[12]M. Nave and J. Wesson, Nucl. Fusion **30**, 2575 (1990).

[13]R. Fitzpatrick, Nucl. Fusion **33**, 1049 (1993).

[14]T. H. Jensen, A. W. Leonard, and A. W. Hyatt, Phys. Fluids B **5**, 1239 (1993).

[15]J. M. Finn and C. R. Sovinec, Phys. Plasmas **5**, 461 (1998).

[16]S. C. Guo and M. S. Chu, Phys. Plasmas **8**, 3342 (2001).

[17]S. C. Guo and M. S. Chu, Phys. Plasmas **9**, 4685 (2002).

[18]C. Gimblett and R. Peckover, Proc. R. Soc. London, Ser. A **368**, 75 (1979).

[19]R. Buttery and G. Giruzzi, Plasma Phys. Controlled Fusion **42**(12B), B61 (2000).

[20]C. G. Gimblett, Plasma Phys. Controlled Fusion **31**, 2183 (1989).

[21]C. G. Gimblett and R. J. Hastie, Phys. Plasmas **7**, 5007 (2000).

[22]M. V. Umansky, R. Betti, and J. P. Freidberg, Phys. Plasmas **8**, 4427 (2001).

[23]C. C. Hegna, Phys. Plasmas **11**, 4230 (2004).

[24]R. Fitzpatrick and A. Aydemir, Nucl. Fusion **36**, 11 (1996).

[25]S. I. Krasheninnikov, L. E. Zakharov, and G. V. Pereverzev, Phys. Plasmas **10**, 1678 (2003).

[26]C. Paz-Soldan, M. I. Brookhart, A. T. Eckhart, D. A. Hannum, C. C. Hegna, J. S. Sarff, and C. B. Forest, Phys. Rev. Lett. **107**, 245001 (2011).

[27]W. F. Bergerson, D. A. Hannum, C. C. Hegna, R. D. Kendrick, J. S. Sarff, and C. B. Forest, Phys. Rev. Lett. **101**, 235005 (2008).

[28]G. Fiksel, A. F. Almagri, D. Craig, M. Iida, S. C. Prager, and J. S. Sarff, Plasma Sources Sci. Technol. **5**, 78 (1996).

[29]D. Hannum, "*Characterizing the plasma of the rotating wall machine*," Ph.D. dissertation (University of Wisconsin-Madison, Madison, WI, 2010).

[30]I. H. Hutchinson, Plasma Phys. Controlled Fusion **43**, 145 (2001).

[31]N. C. Logan, E. J. Strait, and H. Reimerdes, Plasma Phys. Controlled Fusion **52**, 045013 (2010).

[32]D. Gates and T. Hender, Nucl. Fusion **36**, 273 (1996).

[33]C. Paz-Soldan, M. I. Brookhart, A. J. Clinch, D. A. Hannum, and C. B. Forest, Phys. Plasmas **18**, 052114 (2011).

[34]M. Kruskal and M. Schwarzschild, Proc. R. Soc. London, Ser. A **223**, 348 (1954).

[35]V. Shafranov, At. Energ. **5**, 38 (1956).

[36]G. L. Delzanno, E. G. Evstatiev, and J. M. Finn, Phys. Plasmas **14**, 092901 (2007).

[37]V. A. Svidzinski, V. V. Mirnov, and H. Li, Phys. Plasmas **15**, 092106 (2008).

[38]G. L. Delzanno, E. G. Evstatiev, and J. M. Finn, Phys. Plasmas **14**, 072902 (2007).

[39]F. Arcudi, G. L. Delzanno, and J. M. Finn, Phys. Plasmas **17**, 062106 (2010).

[40]W. B. Kunkel, Phys. Fluids **27**, 2369 (1984).

[41]V. Pustovitov, Nucl. Fusion **51**, 013006 (2011).

[42]Z. Yan, M. Xu, P. H. Diamond, C. Holland, S. H. Mller, G. R. Tynan, J. H. Yu, and S. H. Müller, Phys. Rev. Lett. **104**, 10 (2010).